The Astrophysical Journal, 713:1192–1206, 2010 April 20 doi:10.1088/0004-637X/713/2/1192

KINETIC TEMPERATURES OF THE DENSE GAS CLUMPS IN THE ORION KL MOLECULAR CORE

Kuo-Song Wang[1,4], Yi-Jehng Kuan[1,2], Sheng-Yuan Liu[1], and Steven B. Charnley[3]
[1] Institute of Astronomy and Astrophysics, Academia Sinica, P.O. Box 23-141, Taipei 106, Taiwan; kswang@asiaa.sinica.edu.tw
[2] Department of Earth Sciences, National Taiwan Normal University, 88 Sec. 4, Ting-Chou Road, Taipei 116, Taiwan
[3] Astrochemistry Laboratory & Center for Astrobiology, Solar System Exploration Division, Code 691, NASA Goddard Space Flight Center, Greenbelt, MD 20771, USA
Received 2009 June 16; accepted 2010 March 8; published 2010 March 31

ABSTRACT

High angular-resolution images of the $J = 18_K$–17_K emission of CH_3CN in the Orion KL molecular core were observed with the Submillimeter Array (SMA). Our high-resolution observations clearly reveal that CH_3CN emission originates mainly from the Orion Hot Core and the Compact Ridge, both within $\sim$15″ of the warm and dense part of Orion KL. The clumpy nature of the molecular gas in Orion KL can also be readily seen from our high-resolution SMA images. In addition, a semi-open cavity-like kinematic structure is evident at the location between the Hot Core and the Compact Ridge. We performed excitation analysis with the "population diagram" method toward the Hot Core, IRc7, and the northern part of the Compact Ridge. Our results disclose a non-uniform temperature structure on small scales in Orion KL, with a range of temperatures from 190–620 K in the Hot Core. Near the Compact Ridge, the temperatures are found to be 170–280 K. Comparable CH_3CN fractional abundances of 10^{-8} to 10^{-7} are found around both in the Hot Core and the Compact Ridge. Such high abundances require that a hot gas phase chemistry, probably involving ammonia released from grain mantles, plays an important role in forming these CH_3CN molecules.

Key words: ISM: individual objects (Orion KL) – ISM: kinematics and dynamics – ISM: molecules – radio lines: ISM

Online-only material: color figure

1. INTRODUCTION

The Orion KL molecular core is known to be the nearest and most extensively studied massive star-forming region in our Galaxy (see Genzel & Stutzki 1989; O'dell 2001, for review). The kinematic structure of Orion KL was separated spectrally into three major components: they are the "hot core," "ridge," and "plateau" (Blake et al. 1987). The aperture-synthesis study later of Orion KL by Wright et al. (1996) unveiled the fact that all the spectral features recognized in previous studies actually correspond to spatially distinct sources in this molecular core. Consequently these spectral components were classified spatially as the "Ridge," "Compact Ridge," "North Cloud," "Hot Core," "Western Clump," "low-velocity component," and "high-velocity component" (Wright et al. 1996).

Complex organic molecules were also found in the Orion KL region from early spectral-line surveys (e.g., Blake et al. 1987; Wright et al. 1996). Marked chemical differentiation is apparent between the Hot Core and the Compact Ridge with a projected separation of $\sim$8″ to $\sim$10″ between the two. While the Hot Core is rich in nitrogen-bearing molecules (e.g., NH_3, CH_3CN, C_2H_5CN, etc.), the Compact Ridge is rich in oxygen-bearing molecules (e.g., CH_3OH, CH_3OCH_3, $HCOOCH_3$, etc.). Chemical models have been proposed to explain the chemical diversity seen in the Orion KL complex (Blake et al. 1987; Brown et al. 1988; Millar et al. 1991; Charnley et al. 1992; Hasegawa et al. 1992; Caselli et al. 1993; Rodgers & Charnley 2001). In hot core chemistry models, neutral–neutral reactions can play an important role because of the high-temperature environment (van Dishoeck & Blake 1998). Therefore, measurements of the gas temperature, as well as its gradients and structure, are essential to understand both the physics and the chemistry of this cloud core.

Methyl cyanide is a symmetric-top molecule with a large dipole moment (3.91 Debyes) whose *K*-ladders in rotational levels can be excited solely by collisions. Hence CH_3CN can be used to probe the kinetic temperature of molecular clouds (Boucher et al. 1980). Based on the observations at 1 mm to 3 mm of CH_3CN $J = 6$–5 ($\sim$2.″7 beam at 110 GHz) up to $J = 16$–15 ($\sim$1.″1 beam at 294 GHz), comprehensive statistical equilibrium (SE) calculations were employed to estimate the kinetic temperatures of the Hot Core (275 $\pm$ 25 K), and of the quiescent ridge gas (95 $\pm$ 8 K), with a derived fractional abundance $X(CH_3CN)$ ranging from 1.8×10^{-11} to 2.6×10^{-10} (Loren & Mundy 1984). From the 1.3 mm band scan of the OMC-1 cloud between 215 and 263 GHz with a beam size of $\sim$30″ (Sutton et al. 1985; Blake et al. 1986), Sutton et al. (1986) derived a gas temperature of $\sim$275 K for the case of optically thin emission, and $\sim$240 K in the case of photon-trapping; the CH_3CN column density was determined to be 4.6×10^{14} cm^{-2}. Nonetheless, the small-scale structure of the Orion KL complex, which lies within $\sim$30″ of the OMC-1 compact core, was not spatially resolved by the above single-dish studies.

Wilner et al. (1994) first conducted 4″–6″ high-resolution observations of Orion KL using the Berkeley–Illinois–Maryland Association (BIMA) array and imaged the CH_3CN $J = 5$–4 emission at 92 GHz; it was found that CH_3CN 5_4–4_4 emission with $E_u = 127$ K is confined to a compact region of the size of $\sim$10″ near IRc2. A kinetic temperature $\gtrsim$250 K in the Hot Core region and a temperature in the range of 120–170 K toward the southern Compact Ridge were derived via an SE analysis. A corresponding CH_3CN column density of $\sim 5.5 \times 10^{15}$ cm^{-2}, which is about an order of magnitude higher than those derived

[4] Current address: Leiden Observatory, Leiden University, P.O. Box 9513, NL-2300 RA Leiden, The Netherlands.

from single-dish observations, was also obtained (Wilner et al. 1994). More recently, an even higher temperature (600 ± 200 K) was reported in the Orion Hot Core from arcsecond-resolution Submillimeter Array (SMA) observations of CH_3CN J = 37–36 (K = 0–3) at 680 GHz (Beuther et al. 2006).

The large antenna beams of early single-dish measurements (∼0.″5–2.″7) clearly tended to underestimate the gas temperatures in Orion KL. On the other hand, the early BIMA 3 mm observations of CH_3CN transitions, with upper-energy levels E_u < 130 K, suffered from angular resolutions of ∼5″, which are probably insufficient to reveal the fine temperature structure of the chemically active regions around the Hot Core. The recent arcsecond-resolution 440 μm SMA observations of CH_3CN, with E_u = 620–690 K, preferentially sampled the densest and hottest gas clumps, and so were insensitive to the more diffuse and extended methyl cyanide emission, and hence the associated temperature structure.

To elucidate the detailed gas temperature structure within the Orion KL cloud core, we therefore observed the CH_3CN transitions at 331 GHz using the SMA with a resolution of ∼1.″6 × 0.″9. Our SMA observations have sufficient resolution to resolve the two major components, the Hot Core and the Compact Ridge. With K-level up to 8, the nine CH_3CN J = 18–17 transitions observable in our spectral setup cover a wide range of upper-energy levels from ∼ 150 K to 600 K. Such high excitation levels allow us to pick up the warmer and denser gas clumps in Orion KL more easily and thus enable us to measure the corresponding gas temperatures of these hot dense clumps for the first time.

2. CH_3CN SPECTROSCOPY

The rotational state of a symmetric rotor is characterized by two quantum numbers: the total angular momentum, J, and the projection of J on the axis of molecular symmetry, K. Since CH_3CN is highly prolate, at a given J the energy levels at different K increase rapidly with K. The K-state energy levels of adjacent J are nearly the same in general yet modified by the centrifugal distortion which shifts the transition frequency slightly. Hence a single spectrometer setting would simultaneously cover a large number of transitions of the same J-levels but of different K-ladders. As a consequence, calibration errors arising from different observing setups are largely avoided or minimized.

CH_3CN has a three-fold symmetry about the symmetric axis; this symmetry requirement divides the molecule into two distinct species, A and E, distinguishable from the nuclear spin states of hydrogen nuclei in the methyl group. Rotational states with K = 0, 3, 6, ... belong to the A symmetry, and the ones with K = 1, 2, 4, 5, ... are of E symmetry. These two types of symmetry can be treated as if they are of two totally different molecules since the change in nuclear-spin state via collision is negligible and is forbidden via radiative transition. In a warm environment ($\gtrsim$40 K; see Figure 4 of Sutton et al. 1986), the formation ratio of A- to E-type species is expected to be unity. However, in a cold environment such as in the Taurus molecular cloud, the ratio would be greater than unity due to fractionation (Minh et al. 1993; Willacy et al. 1993).

A symmetric top has no permanent electric dipole moment perpendicular to the symmetric axis, hence the angular momentum along this axis cannot be altered via radiative transitions. In other words, the electric dipole selection rules prohibit radiative transitions from changing K. The population distribution over different K for a given J hence can only be modified by collisions. Therefore, a symmetric-top molecule, like CH_3CN, acts as a good probe for measuring gas kinetic temperature as long as the relevant energy states are thermalized. Further hyperfine splitting at each (J, K) level, caused by the nitrogen atom (nuclear spin I = 1), can be neglected because the frequency splitting is very small compared to the spectral resolution of our observations.

3. OBSERVATIONS

Orion KL was observed with the SMA[5] at 342 GHz in 2004 December 03. The observations were carried out with six antennae in the compact-north configuration in an excellent weather condition, with the zenith opacity $\tau_{225\ GHz}$ ∼ 0.03–0.05 and with typical double-sideband system temperatures between 150 K and 350 K. The projected baselines range from ∼15 kλ to ∼150 kλ in length. A uniform source of an angular size greater than ∼14″ or a linear size ∼6300 AU at 450 pc, the distance to Orion KL, would be filtered out by the interferometer.

The phase tracking center was chosen at α_{J2000} = $5^h35^m14^s.48$, δ_{J2000} = −5°22′36.″57, which is roughly midway between the Hot Core and the Compact Ridge. The nominal LSR velocity adopted for observation was 8.0 km s^{-1}. The quasars 0423–013 and 0530+135, which were about 18° and 19° away from Orion KL, respectively, were frequently observed for phase and gain calibrations. Mars was used as the bandpass calibrator, and Uranus, the flux calibrator. The flux error is estimated to be within 30%. The spectral resolution applied is 0.406 MHz per channel or 0.356 km s^{-1} per channel. The target CH_3CN lines were put in the lower sideband (LSB).

Data reduction was conducted by using the MIR package (Scoville et al. 1993) adapted for the SMA, while spectral imaging was performed via MIRIAD (Sault et al. 1995). Uniform weighting was adopted for all mapping for better uv-coverage sampling; the synthesized beam thus obtained is of 1.″6 × 0.″9 (720 AU × 405 AU). The HPBW of the SMA primary beam at 331 GHz is ∼38″. Table 1 gives the rest frequencies of the CH_3CN $J = 18_K$–17_K transitions; also listed are the rest frequencies of the $CH_3{}^{13}CN$ $J = 18_K$–17_K transitions.

4. RESULTS

4.1. Continuum at 331 GHz

Figure 1(a) shows the 331 GHz line-free continuum emission of Orion KL. Strong continuum emission can be seen toward the Hot Core with a peak intensity at ∼1.6 Jy beam^{-1} (∼12 K), while weaker continuum is visible near the Compact Ridge. At arcsec resolution, the Hot Core is resolved partially. Known radio and infrared sources (cf. Shuping et al. 2004; Beuther et al. 2004) are marked by filled circles together with the 331 GHz continuum.

4.2. The Spatial Distribution of CH_3CN

Integrated-intensity maps of CH_3CN J = 18–17 transitions are presented in Figures 1(b)–(h). CH_3CN emission is spatially well-resolved, at arcsec resolution, into the Hot Core, the Compact Ridge, and the Western Clump; similar spatial distributions are found among CH_3CN transitions of various K-ladders with

[5] The SMA is a joint project between the Smithsonian Astrophysical Observatory and the Academia Sinica Institute of Astronomy and Astrophysics, and is funded by the Smithsonian Institution and the Academia Sinica.

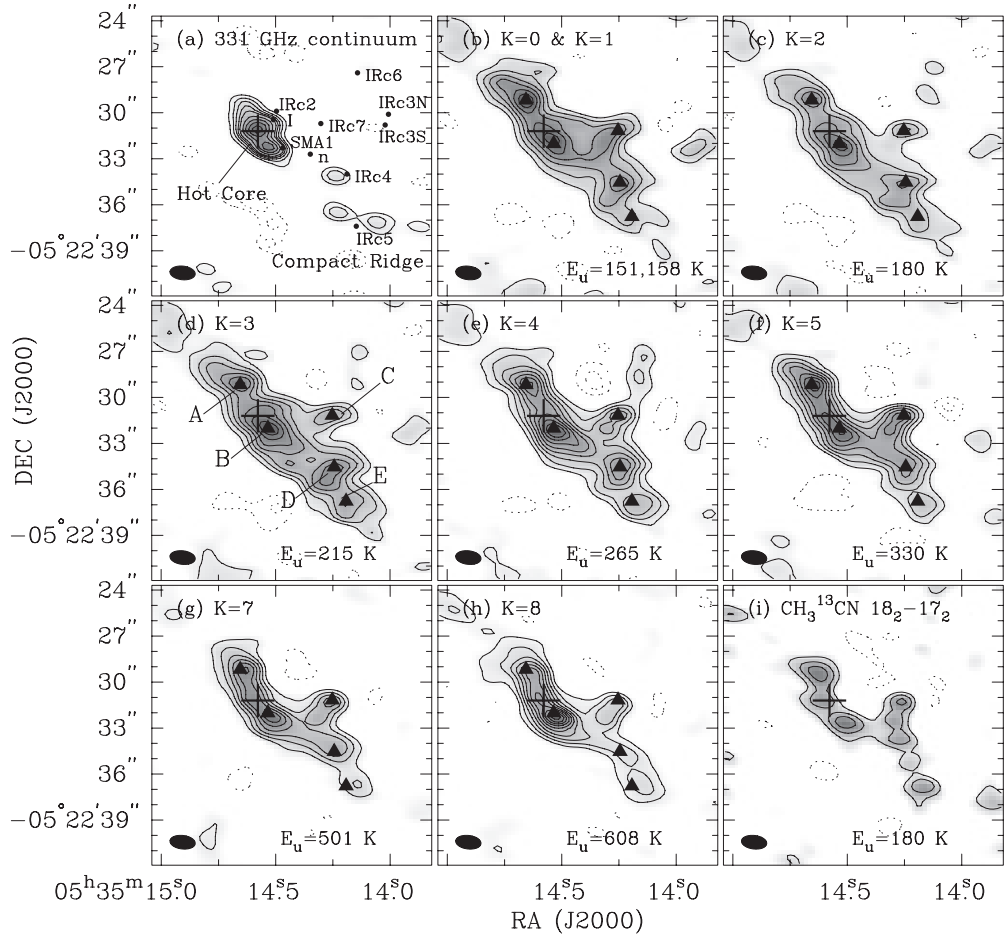

Figure 1. Continuum map of the Orion KL hot molecular core at 331 GHz and the integrated intensity maps of CH_3CN $J = 18$–17 transitions. (a) Continuum at 331 GHz. 1σ noise level is of 0.06 Jy beam^{-1}. Contour levels are at -5σ, -3σ, 3σ, 5σ, 7σ, 9σ, 11σ, 15σ, 19σ, 23σ, and 27σ. The cross marks the continuum peak position. Filled circles indicate the positions of radio and infrared sources in this region (Shuping et al. 2004; Beuther et al. 2004). (b)–(h) Integrated intensity maps of CH_3CN $J = 18$–17 transitions. 1σ noise levels are of 8, 5, 5, 4, 4, 3 and 2 Jy beam^{-1} km s^{-1} in panels (b)–(h), respectively. In panel (f), weak emission from the $CH_3{}^{13}CN$ 18_0–17_0 transition is blended partially with the CH_3CN 18_5–17_5 emission. In panel (h), the $^{34}SO_2$ $21_{2,20}$–$21_{1,21}$ transition, as the potential interloper, may contribute emission to the CH_3CN 18_8–17_8 transition. Contours start at 3σ with 2σ steps. Filled triangles, labeled as A, B, C, D, and E with decreasing right ascension, denote the positions of the sampled spectra. (i) The integrated intensity map of $CH_3{}^{13}CN$ 18_2–17_2 transition. 1σ noise level is of 1 Jy beam^{-1} km s^{-1}. Contours start at 3σ with 2σ steps. The synthesized beam size is of $\sim 1\farcs6 \times 0\farcs9$ with a position angle (P.A.) of $\sim 84°$, and is shown in the lower left corner of each panel. In all panels, solid lines represent positive contours, and dotted lines, negative contours.

different upper energy levels. Note that our data basically resemble the source structure near the Hot Core observed by Wilner et al. (1994). However, significant sub-structure is resolved at arcsec resolution. The emission from CS1 is beyond our field of view. Prominent intensity peaks of CH_3CN emission, marked by the filled triangles, are denoted in Figure 1(d) as A, B, C, D, and E, with decreasing right ascension. Among the five CH_3CN peaks, A and B are closely related to the Hot Core; C is associated with the infrared source IRc7 which is merely $\sim 1''$ away; D and E are in the region corresponding to the northern part of Compact Ridge. Our temperature measurements at D and E in this paper should be treated as an approximation toward the Compact Ridge where HCOOH emission stems (Liu et al. 2002).

Overall, CH_3CN emission of different K-ladders is confined in an NE-SW strip of $\sim 18''$ in length, as shown in Figure 1. This ridge-like structure at $\sim 45°$ position angle extends $\sim 6''$ to the northeast and $\sim 12''$ to the southwest of the Orion Hot Core. A closer look at the southwest extension of the emission from the Hot Core reveals that CH_3CN emission actually extends into the southern region where the Compact Ridge is located. CH_3CN emission from the higher energy states (e.g., 18_7–17_7 and 18_8–17_8) is found to be more compact toward the Hot Core and is stronger than that of the Compact Ridge. Also shown in Figure 1(i) is the spectral emission of the 18_2–17_2 transition of the isotopologue $CH_3{}^{13}CN$; the spatial distribution of its emission appears to be very similar to that of CH_3CN.

By convolving with a $22''$ beam and comparing to the Caltech Submillimeter Observatory spectral-line survey of Orion KL (Schilke et al. 1997), we found our interferometer observations suffer from 65% missing flux in the worst case for the 18_0–17_0 transition ($E_u \sim 150$ K) to 35% missing flux for the 18_8–17_8 transition ($E_u \sim 600$ K). Obviously, spectral emission from higher CH_3CN transitions originates from the more compact regions in Orion KL.

4.3. A Complicated Velocity Field and a Cavity-like Structure

Figures 2 and 3 show the velocity channel maps of CH_3CN $J = 18_3$–17_3 and 18_7–17_7 transitions, respectively. These channel maps are smoothed from the original resolution of 0.36 km s^{-1} ch^{-1} to 1.42 km s^{-1} ch^{-1} by four-channel binning. It is apparent that the overall kinematical motion, hence the physical velocity range, of the molecular gas in Orion KL is quite large (~ 21 km s^{-1}), as reflected by the

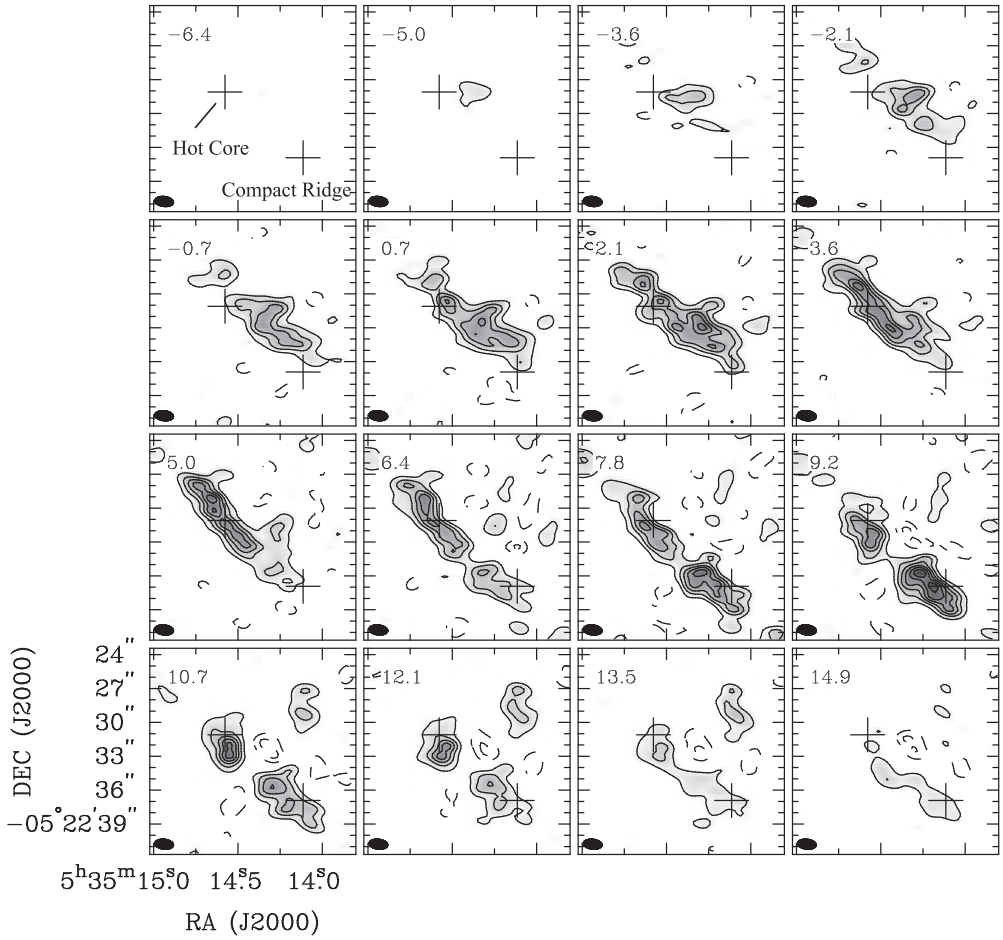

Figure 2. Channel maps of the CH_3CN 18_3–17_3 transition. The channel width is smoothed to ∼1.4 km s^{-1} in velocity. Contours start at 3σ with 4σ step. The 1σ noise level is estimated to be of 0.5 Jy beam^{-1}. Solid lines represent positive contours, and dashed lines, negative contours. LSR velocity in km s^{-1} is shown in the upper left corner of each panel. The angular size of the synthesized beam is of ∼1.″6 × 0.″9 with a P.A. ∼ 84°, as shown in the lower-left corner of each channel. The cross in the north indicates the 331 GHz continuum peak position at the Hot Core, while the southern cross marks a position in the Compact Ridge for reference.

Table 1
Spectral Parameters of Methyl Cyanide $J = 18$–17 Transitions

Molecule	Transition $K =$	ν_0[a] (MHz)	E_u[b] (K)	S_{ul}
CH_3CN	0	331071.6	151	18.0
	1	331065.2	158	17.9
	2	331046.1	180	17.8
	3	331014.3	215	17.5
	4	330969.8	265	17.1
	5	330912.6	330	16.6
	6	330842.7	408	16.0
	7	330760.3	501	15.3
	8	330665.2	608	14.4
$CH_3{}^{13}CN$	0	330907.7	151	18.0
	1	330901.4	158	17.9
	2	330882.4	180	17.8
	3	330850.7	215	17.5
	4	330806.4	265	17.1

Notes.
[a] Rest frequency; adopted from JPL Molecular Spectroscopy at http://spec.jpl.nasa.gov/.
[b] Upper energy level.
[c] Line strength.

CH_3CN emission (Figure 2). Contrary to the wide velocity dispersion of the gas cloud disclosed by the 18_3–17_3 CH_3CN emission, a narrower velocity coverage of ∼14 km s^{-1} of the Orion KL cloud is reflected by the CH_3CN 18_7–17_7 emission (Figure 3). Comparisons of the 18_3–17_3 and 18_7–17_7 channel maps indicate that minor but noticeable morphological differences in CH_3CN emission distribution are present near the Hot Core and the Compact Ridge. For instance, small-scale distribution differences are notable in the channel maps at V_{LSR} from +6.4 to +9.2 km s^{-1} near the Compact Ridge between Figures 2 and 3. Both the narrower velocity range and the small-scale differences in emission morphology can be attributed to, most likely, the higher excitation required for the 18_7–17_7 transition.

The evident extension of CH_3CN emission from the Hot Core region toward the southwestern corner of the map near the Compact Ridge discloses the complicated nature of the velocity field in Orion KL. To illustrate the complexity of the velocity field, two reference positions, one at the continuum peak of the Hot Core and the other near the Compact Ridge, were selected and marked with crosses in both Figures 2 and 3. The CH_3CN emission is clearly elongated in the NE–SW direction roughly connecting the two reference crosses. Immediately we see the distribution of CH_3CN emission circumventing the southern reference cross near the Compact Ridge with increasing LSR velocity (Figure 2). In other words, the southwest end of the CH_3CN molecular distribution moves around the southern reference cross from its north to its east, then moves to its

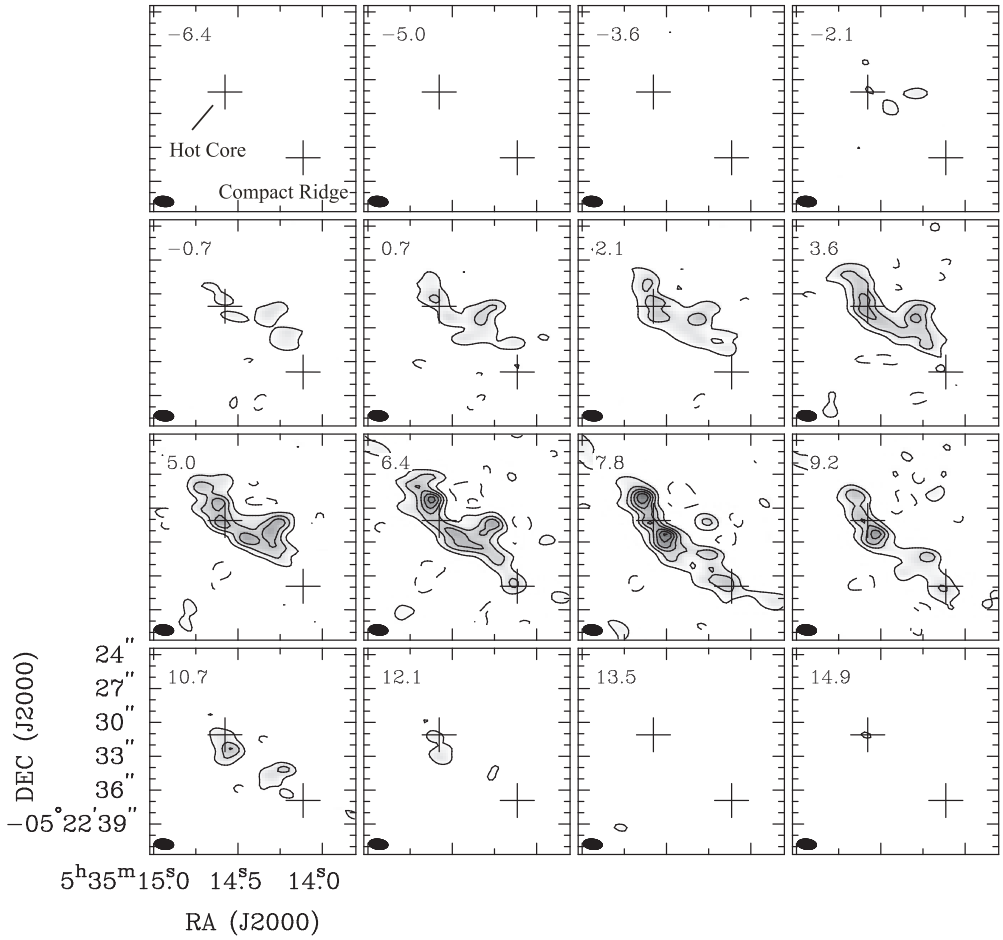

Figure 3. Channel maps of the CH_3CN 18_7–17_7 transition. The same figure convention employed in Figure 2 is adopted here, except that the 1σ noise level is estimated to be of 0.3 Jy beam^{-1}.

south, as the LSR velocity increases from $V_{\rm LSR} = -2.1$ to +14.9 km s^{-1}; this suggests the likely existence of a semi-open gas cavity structure with lower density in the region between the Hot Core and the Compact Ridge. This semi-open cavity can be seen in the channel maps (Figure 2) at velocity from 5.0 km s^{-1} to 14.9 km s^{-1}. Low emission is seen near the position at the center between our two reference crosses.

To further investigate the semi-open cavity-like structure indicated in the channel maps, position–velocity (P–V) diagrams (Figure 4) were obtained according to the six position cuts A–B, A–C, A–D, B–C, B–D, and C–D along the lines connecting the four emission peaks A, B, C, and D, as shown in Figure 1(d), in pairs. The zero offset in position in each P–V diagram marks the midway position between each pair of the CH_3CN emission peaks connected.

An obvious void of V-shape morphology, outlined by thick dashed lines in Figure 4, is visible in most of the P–V diagrams shown in the velocity range starting from ∼6 km s^{-1} and up to ∼15 km s^{-1}, especially in the position cuts of A–D, B–C, and B–D. Clearly, this V-shape morphology implies the existence of a southwest semi-open gas cavity between the Hot Core and the Compact Ridge. Furthermore, cuts A–B and C–D also show, though less conspicuous, evidences of the existence of such semi-open gas cavity.

In addition to the cavity in the gas cloud near the Compact Ridge, another gas cavity may also be present in the northwest direction of the Hot Core, as indicated by the morphology of CH_3CN emission north and west of the Hot Core (Figure 1) and by the position–velocity diagram of the slice A–C outlined by the dotted-dashed line in Figure 4. This NW semi-open gas cavity is most likely due to a poorly collimated outflow originated from a region NW of the Hot Core. More detailed discussion of the SW semi-open cavity-like structure will be given in Section 5.3.

4.4. Line-profile Fitting and Different Excitation Zones

Figure 5 shows the spectra, from the top to the bottom, taken at the five representative positions from A to E, respectively. In order to study the detailed excitation conditions in Orion KL at small scales, Gaussian line-profile fitting was first applied to derive line parameters. For each CH_3CN line, we obtained the LSR velocity $V_{\rm LSR}$, the FWHM line width ΔV, and the velocity integrated line intensity $W = \int I_v dv$, where I_v is the line intensity and v is the velocity. In fitting the profiles at a given position, all CH_3CN lines were assumed to be at the same LSR velocity and to have the same line width. At positions B, C, and D, where their line profiles are double-peak, the line widths of each pair of velocity components were manually fixed in order to have reasonable fits. However, due to severe line blending, line-profile fittings of the tightly adjacent $K = 0$ and 1 lines were not attempted for those double-peak cases. Imposition of the above conditions reduced the amount of freedom in fitting the line profiles. Similar fitting assumptions were also applied to the $CH_3{}^{13}CN$ 18_K–17_K lines.

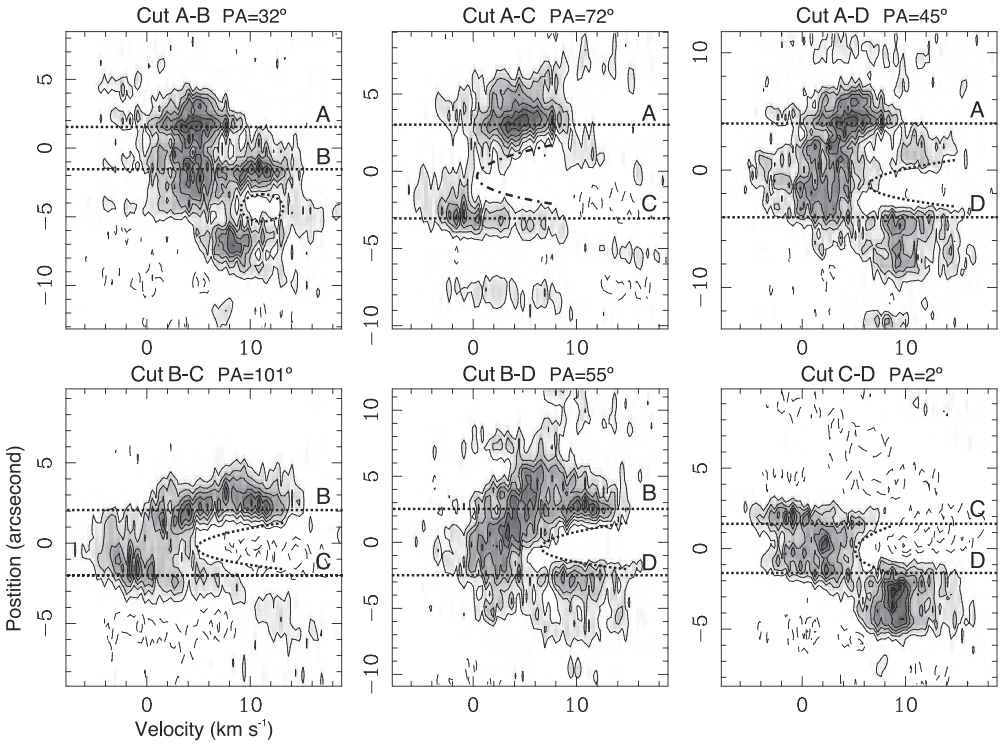

Figure 4. CH_3CN 18_3–17_3 position–velocity diagrams in the Orion KL region. Position–velocity cuts were taken along the CH_3CN emission peak positions shown in Figure 1(d). The zero position offset marks the midway between each pair of CH_3CN emission peaks connected. The locations of the position pair are marked with dotted lines in each panel. The position angle (P.A.) of the P–V cut is also listed in each P–V diagram with positive position offsets to the P.A. direction, while negative offsets indicating the direction opposite to that of the P.A. Contours start at 3σ in 3σ steps, with one σ at 0.4 Jy beam^{-1}; negative contours are displayed with thin long-dashed lines. Thick dashed lines mark the apparent existence of the cavity structure located between the Hot Core and the Compact Ridge. The thick dotted-dashed line denoted in the cut A–C represents another cavity-like structure situated in the NW direction of the Hot Core.

The assumption of fixed line width helps to get self-consistent solutions (assuming all *K*-transitions are from similar bulk of gas) and to reduce the degree of freedom in the Gaussian decomposition of the complex spectra observed, especially for those positions with apparently double peak. We note that the Gaussian decompositions toward the double-peak position (B, C, and D) may not be unique. If we let the line width of each *K* transition of each velocity component to be the free parameter, we may get a set of non-selfconsistent line width for each velocity component. We also note that the line width for lower *K*-transitions could be greater than those for higher *K*-transitions (see Figure 6). The error in line width, hence the estimation of optical depth (Equation (4)) in our population diagram (PD) analysis, is estimated conservatively to be ∼20%. However, with the consideration of error in line width, our results derived from the PD analysis do not change much. As a result, we adapted the fixed line width assumption in our fit.

The $K = 6$ line of CH_3CN was excluded from the line fitting because of the likely spectral blending with the HNCO $15_{1,14}$–$14_{1,13}$ emission at 330848.8 MHz and the 18_3–17_3 transition of $CH_3{}^{13}CN$ at 330850.7 MHz. The $K = 8$ line of CH_3CN, on the other hand, may be contaminated by the $21_{2,20}$–$21_{1,21}$ emission of $^{34}SO_2$ at 330667.8 MHz. No effort was made to include the $CH_3{}^{13}CN$ 18_0–17_0 transition while fitting the $K = 5$ line of CH_3CN. The individual Gaussian-fitted line components and their synthesized spectra at the five positions are shown in Figure 5.

Tables 2 and 3 summarize the fitted line parameters of CH_3CN and $CH_3{}^{13}CN$ spectra, respectively. In both tables, Columns 1–4 are the name of the subsource in Orion KL, the position where the spectrum was sampled, the line center LSR velocity, and the FWHM line width, respectively. Because most of the CH_3CN transitions exhibit double-line profiles at positions B, C, and D, to separate the blueshifted and redshifted components spectrally, the subscripts "blue" and "red" are adopted to distinguish the two velocity components at each position. Therefore, for example, we have positions B_{blue} and B_{red}. The remaining columns (5–12 in Table 2; 5–7 in Table 3) indicate the velocity integrated intensity of different *K*-ladders. At all five positions sampled, our assumption of an identical LSR velocity for all CH_3CN *K*-ladders at the same position did not yield reasonably good fits for the $K = 7$ and 8 lines. Such an inconsistency can be best illustrated by Figure 6 where the enlarged CH_3CN $K = 7$ lines taken at all five positions are compared to their $K = 4$ counterparts.

In Figure 6, the fitted LSR velocity, in km s^{-1}, of each line component is shown in the upper left parentheses of each spectrum. It can be seen, at position A, the $K = 7$ line appears to be ∼1.0 km s^{-1} redshifted with respect to the $K = 4$ line or other low *K* CH_3CN lines. At position B, on the contrary, both line components of the $K = 7$ line are blueshifted ∼2.0 km s^{-1} with respect to the $K = 4$ lines. Toward position C, only the redshifted peak of the $K = 7$ line shows a further redshift of ∼1.0 km s^{-1} compared to the one of the $K = 4$ line; nonetheless, no significant velocity offset was observed in the blueshifted components of both $K = 4$ and $K = 7$ lines. At position D, a blueshifted velocity offset of ∼1.0 km s^{-1} was found, similar to the situation occurred at position B. Likewise, at position E, the $K = 7$ line appeared to be ∼1.0 km s^{-1} blueshifted with respect to the $K = 4$ line. The nontrivial velocity offsets of the line centers observed between the low-*K* and high-*K* components at all positions thus imply the regions with high excitation,

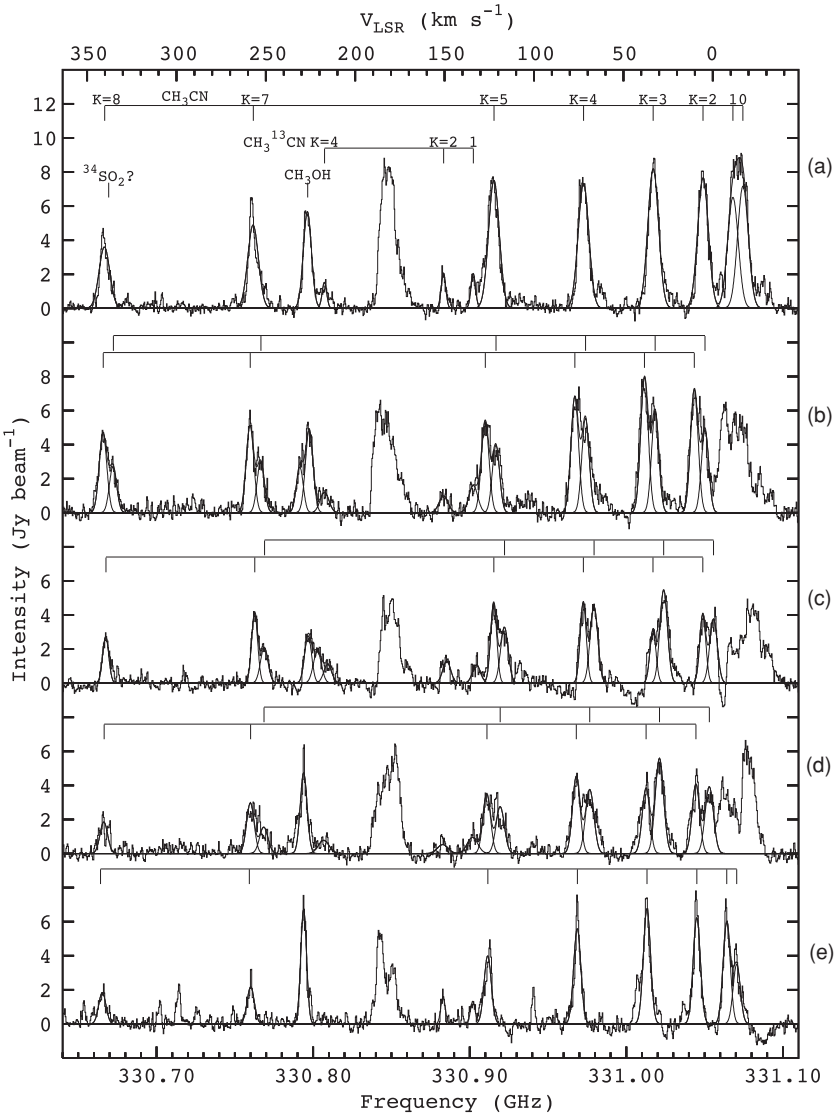

Figure 5. Hanning-smoothed CH_3CN sample spectra in Orion KL. From top to bottom are the spectra, taken at positions, respectively, A, B, C, D, and E shown in Figure 1(d). The labeled LSR velocity is determined according to the rest frequency of the CH_3CN 18_2–17_2 transition. The 1σ noise level is $\sim$0.3 Jy beam^{-1}. Gaussian fittings were applied to all spectra and are shown in smooth, thin lines for each spectral component fitted. The resultant line profiles from adding individual Gaussian fittings are shown in thick lines.

where high K transitions occur, may not be perfectly coincident spatially with the regions where most of the low K emission originates. Figure 6 also gives an example of the remarkable variation of the LSR velocity with positions in the Orion KL cloud core.

4.5. Rotation Diagram Analysis

By assuming LTE with optically thin lines and a source of uniform density and temperature with no background radiation, we can estimate the excitation temperature and column density of a molecular species via a rotation diagram (RD) analysis (Turner 1991). The equation for RD analysis is actually the derivation of the Boltzmann equation,

$$\ln\left(\frac{N_{\rm u}}{g_{\rm u}}\right) = \ln\left(\frac{N_{\rm tot}}{Q_{\rm rot}}\right) - \frac{E_{\rm u}}{kT_{\rm rot}}, \qquad (1)$$

where $N_{\rm u}$ is the molecular column density of the upper state of transition, $g_{\rm u}$ is the total degeneracy of the upper state, $N_{\rm tot}$ represents the total column density of the molecule, $Q_{\rm rot}$ is the dimensionless rotational partition function, $E_{\rm u}$ is the upper energy level, and $T_{\rm rot}$ is the rotational excitation temperature and k is the Boltzmann constant.

For interferometric observations, the left-hand side of Equation (1) can also be estimated via (Miao et al. 1995)

$$\ln\left(\frac{N_{\rm u}^{\rm obs}}{g_{\rm u}}\right) = \ln\left(\frac{2.04\times10^{20}}{\theta_a\theta_b}\frac{W}{g_K g_I \nu_0^3 S_{\rm ul}\mu_0^2}\right), \qquad (2)$$

where $N_{\rm u}^{\rm obs}$, in cm^{-2}, represents the observed column density of the molecule assuming LTE with optically thin line; θ_a and θ_b, in arcsecond, are the major and minor axes, respectively, of the clean beam; W is the integrated intensity in Jy beam^{-1} km s^{-1}; g_K is the K-ladder degeneracy, g_I is the degeneracy due to nuclear spin; ν_0, in GHz, is the rest frequency of the rotational transition; $S_{\rm ul}$ is the line strength of the transition; μ_0, in Debye, is the permanent dipole moment of the molecule. Equation (1) is in fact a linear equation, with $\ln(N_{\rm u}/g_{\rm u})$ being the ordinate, and $E_{\rm u}/k$, the abscissa; the slope of this linear equation is hence $(-1/T_{\rm rot})$, and $\ln(N_{\rm tot}/Q_{\rm rot})$, the intercept. By plotting the data

Table 2
Observed Line Parameters of CH_3CN $J = 18$–17 Transitions

Source	Position	V_{LSR}[b]	ΔV[c]	$\int I_v dv$[a] (Jy beam^{-1} km s^{-1})							
		(km s^{-1})	(km s^{-1})	$K = 0$	$K = 1$	$K = 2$	$K = 3$	$K = 4$	$K = 5$	$K = 7$	$K = 8$
(1)	(2)	(3)	(4)	(5)	(6)	(7)	(8)	(9)	(10)	(11)	(12)
HC[d]	A	5.5(0.1)[e]	7.0(0.2)	53.5(2.8)	48.6(2.8)	57.2(2.5)	61.2(2.5)	54.7(2.5)	56.1(2.5)	36.5(2.4)	26.9(2.4)
	B_{blue}	4.3(0.1)	4.8[f]	···	···	24.8(2.4)	30.3(2.4)	28.4(2.4)	20.2(2.4)	15.3(2.5)	13.9(2.6)
	B_{red}	10.3(0.1)	5.0[f]	···	···	38.5(2.4)	42.3(2.5)	36.1(2.4)	28.5(2.6)	27.2(2.5)	24.9(2.6)
IRc7	C_{blue}	−0.4(0.1)	5.0[f]	···	···	20.0(1.8)	29.1(1.8)	24.0(1.8)	17.4(1.8)	11.1(1.9)	···
	C_{red}	5.6(0.1)	4.0[f]	···	···	17.2(1.6)	13.2(1.6)	20.0(1.6)	20.1(1.6)	17.5(1.7)	11.6(1.8)
n-CR[g]	D_{blue}	2.0(0.2)	5.5	···	···	22.9(2.2)	32.7(2.2)	22.0(2.2)	16.1(2.2)	9.0(2.2)	···
	D_{red}	9.5(0.2)	5.0	···	···	21.6(2.1)	20.4(2.1)	24.1(2.1)	18.6(2.2)	15.8(2.1)	9.9(2.1)
	E	9.0(0.1)	4.7(0.1)	17.6(1.3)	30.0(1.3)	31.5(1.3)	34.1(1.4)	28.2(1.3)	20.1(1.3)	11.0(1.3)	9.3(1.3)

Notes.
[a] Velocity integrated intensity.
[b] LSR velocity at the line center fitted from $K \leqslant 5$ lines. For $K = 7$ and 8 lines, their LSR velocities appear to be offset from those of the low-K lines. See Section 4.4 for details.
[c] FWHM line width.
[d] The Hot Core.
[e] 1σ rms given in the parentheses.
[f] The line width presumed.
[g] The northern part of the Compact Ridge.

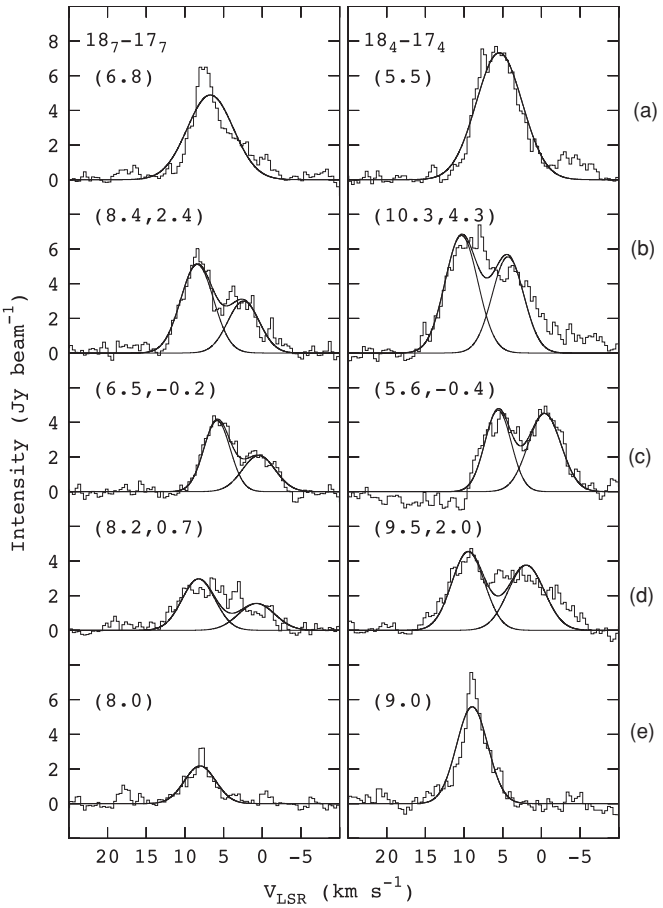

Figure 6. Hanning-smoothed spectra of CH_3CN 18_7–17_7 (left panel) and 18_4–17_4 (right panel) in Orion KL. Spectra shown in each column, from top to bottom, respectively, were taken at positions A, B, C, D, and E shown in Figure 1(d), as indicated by the alphabetic letters on the right-hand side of the figure. The noise level of each spectrum is ∼0.3 Jy beam^{-1}. The numbers shown in the upper left parentheses of each spectrum represent the LSR velocity, in km s^{-1}, of the Gaussian-fitted emission peak of each velocity component. Thin lines denote the Gaussian-fitted spectral components, and thick lines, the resultant line profiles from adding individually fitted Gaussians.

Table 3
Observed Line Parameters of $CH_3{}^{13}CN$ $J = 18$–17 Transitions

Source	Position	V_{LSR}[b]	ΔV[c]	$\int I_v dv$[a] (Jy beam^{-1} km s^{-1})		
		(km s^{-1})	(km s^{-1})	$K = 1$	$K = 2$	$K = 4$
(1)	(2)	(3)	(4)	(5)	(6)	(7)
HC[d]	A	7.3(0.3)[e]	3.0[f]	6.5(1.6)	6.6(1.6)	4.9(1.6)
	B	7.1(0.7)	5.7(1.7)	10.0(3.1)	6.2(2.7)	7.5(2.9)
IRc7	C	5.4(0.6)	5.2(1.3)	6.0(1.9)	7.2(2.0)	6.1(2.9)
n-CR[g]	D	7.6(1.1)	7.0(2.6)	7.0(2.9)	3.9(2.6)	5.8(2.7)
	E	7.4(0.3)	3.0[f]	4.3(1.0)	5.0(1.0)	···

Notes.
[a] Velocity integrated intensity.
[b] LSR velocity at the line center.
[c] FWHM line width.
[d] The Hot Core.
[e] 1σ rms given in the parentheses.
[f] The line width presumed.
[g] The northern part of the Compact Ridge.

points from all transitions measured according to Equation (2) and applying least-square fitting for a straight line, T_{rot} can then be inferred from the reciprocal of the fitted line slope; likewise, N_{tot} can also be obtained from the intercept of the fitted line once T_{rot}, hence Q_{rot}, has been determined.

CH_3CN rotation diagrams at five positions and of different velocity components are shown in Figure 7, where the observational data are denoted by open circles with an error bar in red color. The RD diagrams contain some data points with large deviation from a straight line, in particular, the $K = 3$ lines; this suggests that some of the CH_3CN lines are not optically thin. Thus, the optically thin assumption required by the RD analysis may not be valid.

Moreover, as shown in Figure 5, the peak intensities of the $K = 0$–4 transitions are found to be similar; it also implies that these low K-ladder CH_3CN lines are optically thick. Under LTE conditions, the peak brightness temperature, scaled by the beam–source coupling factor, of an optically thick line would be

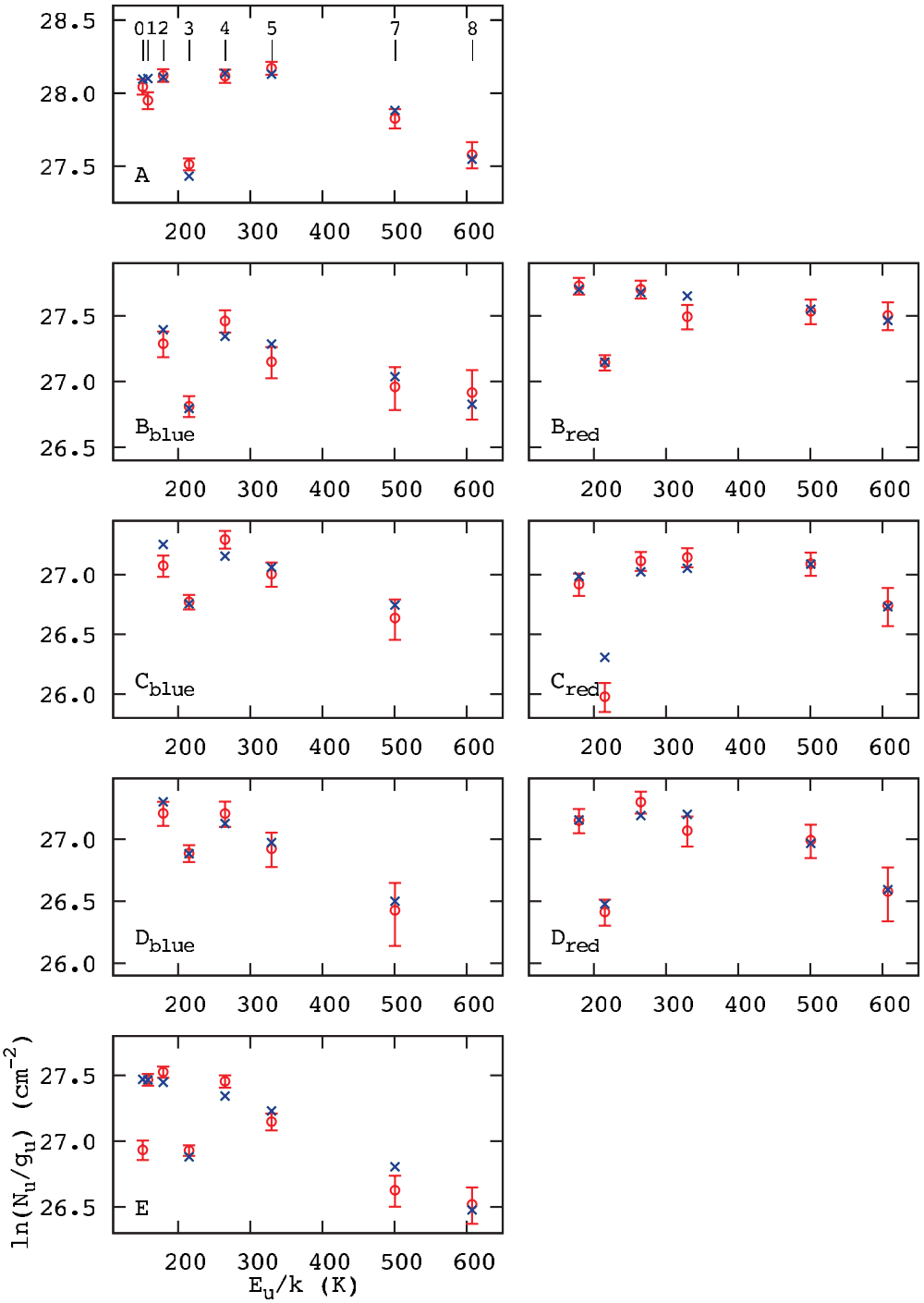

Figure 7. PDs of CH_3CN 18_K–17_K transitions. Open circles in red represent the actual, observed data with error bars. Crosses in blue mark the best-fitted results from PD analysis. The numbers illustrated in the top left panel diagram of position A are the *K*-ladder quantum numbers.

(A color version of this figure is available in the online journal.)

a direct measure of the kinetic temperature of the gas. From our data, the peak intensities of the low *K*-ladder lines at position A are about 8 Jy beam^{-1} which, without beam–source correction, corresponds to a brightness temperature, and hence to a kinetic temperature in LTE, of ∼60 K; a similar kinetic temperature can also be obtained for position E. However, the apparently different peak-intensity ratios between the high *K*-ladder lines, e.g., between the $K = 4$ and $K = 7$, at positions A and E, suggest different kinetic temperatures and CH_3CN gas densities at these two positions. Thus, the physical conditions in clumps A and E must be different than is indicated by the low *K*-ladder data alone. Toward positions B, C, and D, the lower limit kinetic temperatures are estimated to be of 45–60 K.

4.6. Population Diagram Analysis

Taking into account the optical depth effect consequently, and following the method developed by Goldsmith & Langer (1999), we applied the PD analysis to all CH_3CN lines observed.

In the PD analysis, we have

$$\ln\left(\frac{\hat{N}_{\rm u}^{\rm obs}}{g_{\rm u}}\right) = \ln\left(\frac{N_{\rm tot}}{Q_{\rm rot}}\right) - \frac{E_{\rm u}}{kT_{\rm rot}} - \ln\left(\frac{\Omega_a}{\Omega_s}\right) - \ln(C_\tau), \quad (3)$$

where $\hat{N}_{\rm u}^{\rm obs}$ is the observed upper state column density of the target molecule including the line opacity and beam–source coupling effects; Ω_a is the beam solid angle; Ω_s is the solid angle of the source; $C_\tau = \tau/(1-e^{-\tau})$, with τ being the optical depth of the intervening cloud. The ratio of Ω_s/Ω_a is also known as the source filling factor, f. When $\tau \gg 1$, the inferred upper level molecular population would be underestimated by a factor τ. If the source is unresolved, the observed upper-level population would be underestimated by a further factor of f^{-1}. Thus, linear least-square fitting to the level populations, as we did in the RD analysis, would introduce significant errors in the excitation temperature and total molecular column density due to large line opacity.

To correct for the likely deviation introduced by non-trivial line opacity, the line center opacity for CH_3CN can be expressed as

$$\tau = \frac{c^3}{8\pi\nu_0^3}\frac{A_{\rm ul}}{\Delta V}\frac{g_{\rm u}N_{\rm tot}}{Q_{\rm rot}}e^{-\frac{E_{\rm u}}{kT_{\rm rot}}}(e^{\frac{h\nu_0}{kT_{\rm rot}}}-1), \quad (4)$$

where c is the speed of light; $A_{\rm ul}$ is the Einstein-A coefficient of spontaneous emission; ΔV is the line width at FWHM. For CH_3CN, the molecular parameters of $A_{\rm ul}$, $g_{\rm u}$, and $Q_{\rm rot}$ are

$$A_{\rm ul} = \frac{64\pi^4}{3h}\frac{\nu_0^3}{c^3}\frac{\mu_0^2}{2J_{\rm u}+1}\frac{J_{\rm u}^2-K^2}{J_{\rm u}}, \quad (5)$$

$$g_{\rm u} = \begin{cases} \frac{1}{2}(2J_{\rm u}+1), & \text{if } K=0 \\ 2J_{\rm u}+1, & \text{if } K=3,6,9,\ldots \\ \frac{1}{2}(2J_{\rm u}+1) & \text{if } K=1,2,4,5,\ldots \end{cases} \quad (6)$$

and

$$Q_{\rm rot}(T_{\rm rot}) = \frac{1}{3}\sqrt{\frac{\pi(kT_{\rm rot})^3}{h^3AB^2}}, \quad (7)$$

respectively, where h is the Planck constant, $J_{\rm u}$ is the quantum number J of upper state, A and B are the rotational constants. In LTE, the observed upper-level populations, $\hat{N}_{\rm u}^{\rm obs}$, can be predicted according to the right-hand side of Equation (3) for a given set of total column density, $N_{\rm tot}$, rotational temperature, $T_{\rm rot}$, and source filling factor, f. By comparing $\hat{N}_{\rm u}^{\rm obs}$ with $N_{\rm u}^{\rm obs}$ calculated by Equation (2), we thus performed χ^2 minimization:

$$\chi^2 = \sum\left(\frac{N_{\rm u}^{\rm obs}-\hat{N}_{\rm u}^{\rm obs}}{\delta N_{\rm u}^{\rm obs}}\right)^2, \quad (8)$$

where $\delta N_{\rm u}^{\rm obs}$ is the 1σ error of the inferred upper-state column density from observations. The expected $\hat{N}_{\rm u}^{\rm obs}$ were evaluated for the parameter space of $T_{\rm rot}$ = 20–1300 K, $N_{\rm tot}$ in the range of 10^{14}–10^{19} cm^{-2}, and f between 0.01 and 1.0.

The best-fit model populations, $\hat{N}_{\rm u}^{\rm obs}$, at the five different positions A, B, C, D, and E, are marked as cross symbols in blue color and are plotted together with the rotation diagrams in Figure 7. Toward the Hot Core at position A, our PD analysis gave a rotational temperature of ∼190 K, which is slightly lower than the value, ≳250 K, reported by Wilner et al. (1994). Near the Hot Core at position B, the blueshifted component $B_{\rm blue}$ at $V_{\rm LSR}$ = 4.3 km s^{-1} was found to have a rotational temperature of ∼330 K, consistent with the lower limit set by Wilner et al. (1994); however, an even higher excitation temperature of ∼620 K was obtained for the redshifted component $B_{\rm red}$ at $V_{\rm LSR}$ = 10.3 km s^{-1}. The total beam-averaged column densities of CH_3CN among positions A, $B_{\rm blue,}$ and $B_{\rm red}$ near the Hot Core region are thus derived in the range of ∼(1–4) × 10^{16} cm^{-2}. However, if we take the source filling factor into account, the actual CH_3CN column density can be as high as ∼1 × 10^{17} cm^{-2} toward the Hot Core. Near IRc7 at position C, using the PD analysis we obtained $T_{\rm rot}$ = ∼350 K and ∼100 K, respectively, for the $C_{\rm blue}$ component at $V_{\rm LSR}$ = −0.4 km s^{-1} and for the $C_{\rm red}$ component at $V_{\rm LSR}$ = 5.6 km s^{-1}. The beam-averaged column density is ∼0.7 × 10^{16} cm^{-2} for the $C_{\rm blue}$ component and for the $C_{\rm red}$ component, a lower limit of the column density of 1.3 × 10^{16} cm^{-2} was derived. Again, if the source filling factor is considered, the actual column densities will be an order of magnitude higher toward both $C_{\rm blue}$ and $C_{\rm red}$. Toward the northern Compact Ridge at positions D and E, the estimated rotational temperatures are in the range of ∼170–280 K, and the corresponding beam-averaged column densities are in the range of (0.5–2.0) × 10^{16} cm^{-2}; similarly, the actual column densities are an order of magnitude higher than the beam-averaged and are of (0.3–1.0) × 10^{17} cm^{-2}. Table 4 gives a detailed summary of the results from the PD analysis.

Table 4
Summary of the Population Diagram Analysis

Source	Position	$T_{\rm rot}$[a] (K)	$N_{\rm tot}\times\Omega_s/\Omega_a$[b] ($\times10^{16}$ cm^{-2})	Ω_s/Ω_a[c]	$N_{\rm tot}$[d] ($\times10^{17}$ cm^{-2})
HC[e]	A	191^{+96}_{-60}	$3.8^{+4.5}_{-1.1}$	$0.34^{+0.16}_{-0.11}$	$1.1^{+0.6}_{-0.1}$
	$B_{\rm blue}$	333^{+511}_{-135}	$1.1^{+0.7}_{-0.3}$	$0.15^{+0.08}_{-0.08}$	$0.7^{+1.8}_{-0.3}$
	$B_{\rm red}$	$621^{+579\,f}_{-252}$	$2.5^{+2.3}_{-0.7}$	$0.11^{+0.06}_{-0.05}$	$2.2^{+5.7}_{-1.1}$
IRc7	$C_{\rm blue}$	348^{+567}_{-166}	$0.7^{+0.8}_{-0.2}$	$0.14^{+0.10}_{-0.08}$	$0.5^{+2.0}_{-0.2}$
	$C_{\rm red}$	101^{+268}_{-47}	$1.3^{+72.8\,g}_{-1.1}$	$0.38^{+0.42}_{-0.28}$	$3.4^{+89.2\,g}_{-2.5}$
n-CR[h]	$D_{\rm blue}$	283^{+465}_{-110}	$0.5^{+0.5}_{-0.1}$	$0.20^{+0.10}_{-0.11}$	$0.3^{+0.8}_{-0.2}$
	$D_{\rm red}$	168^{+252}_{-100}	$1.9^{+84}_{-1.0}$	$0.21^{+0.33}_{-0.12}$	$0.9^{+14.9}_{-0.3}$
	E	257^{+83}_{-61}	$0.8^{+0.1}_{-0.1}$	$0.22^{+0.05}_{-0.04}$	$0.4^{+0.1}_{-0.1}$

Notes.
[a] Rotational temperature.
[b] The beam-averaged molecular column density.
[c] The source filling factor, or the ratio of source solid angle over beam solid angle.
[d] Total molecular column density corrected for the source filling factor.
[e] The Hot Core.
[f] The inferred upper error is equal to the upper boundary of $T_{\rm rot}$ in χ^2 minimization.
[g] The inferred upper error is equal to the upper boundary of $N_{\rm tot}$ in χ^2 minimization.
[h] The northern part of the Compact Ridge.

Based on our PD analysis, it is evident that the temperature distribution in Orion KL contains large variations not only at small angular scales but also along those lines of sight containing two discernible velocity components. We note that, in all cases, the source filling factors inferred via PD modeling are all consistent with a value less than 0.5. The estimated line center opacities of each K-ladder transition at different positions are listed in Table 5; where it can be seen that the lines with K ladders ⩽3 are optically thick basically.

The line opacities of CH_3CN can also be estimated from the $CH_3{}^{13}CN$ lines in our data. Since we only have three weak, isolated lines of $CH_3{}^{13}CN$ (K = 1, 2 and 4), we are

Table 5
Line Opacities of CH_3CN 18_K–17_K Transitions Derived from Population Diagram Analysis

Transition	Position							
18_K–17_K, K =	A	B_{blue}	B_{red}	C_{blue}	C_{red}	D_{blue}	D_{red}	E
0	8.5	...	...	...	...	...	...	2.3
1	8.1	...	...	...	...	...	...	2.2
2	7.2	2.4	2.0	1.5	85	1.0	9.8	2.0
3	11.8	4.3	3.7	2.7	117	1.8	16	3.5
4	4.4	1.8	1.7	1.1	35	0.7	5.7	1.4
5	3.1	1.4	1.4	0.9	18	0.6	3.7	1.1
7	1.2	0.8	1.0	0.5	3.0	0.3	1.2	0.5
8	0.6	0.5	0.8	...	1.0	...	0.6	0.3

not able to derive the T_{rot}, $N_{tot,}$ and f independently via PD analysis. More than four transitions are needed. Rather, we can estimate the optical depth from the $K = 2$ transition assuming a $^{12}C/^{13}C$ ratio of 60 (Wilson & Rood 1994). Take position A as an example. The low line intensity of $CH_3{}^{13}CN$, $K = 2$ transition directly imply its opacity is low; if it is optically thick, it should have similar line intensity to the CH_3CN, $K = 2$ transition. Assuming $CH_3{}^{13}CN$ has same kinetic temperature measured from CH_3CN, the beam averaged total column density under LTE is derived to be $\sim 2.0 \times 10^{15}$ cm^{-2}, which implies a total column density of $\sim 1.2 \times 10^{16}$ cm^{-2} for CH_3CN. The beam-averaged total column density is estimated to be $\sim 1.7 \times 10^{16}$ cm^{-2} from CH_3CN, $K = 2$ transition under optically thin assumption. A factor of 7 difference implies the line opacity of CH_3CN, $K = 2$ transition is ~ 7, which is generally consistent with the opacity derived from multi-line calculation in PD analysis. In this simple calculation we can see low-K transitions of CH_3CN is basically optically thick.

5. DISCUSSION

5.1. Parameter Degeneracy, Line Opacity, and Small Source Filling Factor

In the PD analysis, there exists degeneracy between the free parameters—T_{rot}, $N_{tot,}$ and f. For a better understanding of the degeneracy, let us consider two extreme cases under LTE condition: all transitions are either optically thin or optically thick. In the optically thin case, the total column density and source filling factor are coupled (i.e., $N_{tot} \times f$ = constant). For example, at a given rotational temperature, a column density of 10^{13} cm^{-2} with $f = 1$ and a column density of 10^{14} cm^{-2} with $f = 0.1$ would both reproduce the observed line flux densities as long as all transitions are optically thin. In this case, total column density and source filling factor cannot be well determined. Only an upper limit of total column density might be found. In the optically thick case, which all transitions have comparable line brightness, rotational temperature and source filling factor are degenerated (i.e., $T_{rot} \times f$ = constant). In other words, for a given high total column density (to ensure that all lines are optically thick), a rotational temperature at 100 K with $f = 1$ and a rotational temperature at 1000 K with $f = 0.1$ would reproduce the observed line intensities. In this case, rotational temperature and source filling factor cannot be well derived. Only a lower limit of rotational temperature can be obtained from the peak line brightness. As a result, in these two extreme cases, the degeneracy between the free parameters cannot be broken. However, if some of the transitions are optically thick and others are optically thin as apparently position A looks like, we may have a chance to break the degeneracy. The N_{tot}–f degeneracy can be broken from those optically thick lines and T_{rot}–f degeneracy can be broken from those optically thin lines. As a consequence, we used χ^2 minimization to find out a set of T_{rot}, $N_{tot,}$ and f that can better fit *both* optically thin and optically thick transitions. The range of each free parameter can be minimized if enough numbers of optically thick and optically thin transitions are present.

It is apparent that, while searching for minimal χ^2 in the PD approach, source filling factors smaller than unity were necessary for achieving good fits; this implies that the intrinsic size of each source component at the five selected positions of Orion KL is in general smaller than the synthesized *clean* beam ($1\farcs6 \times 0\farcs9$). One underlying assumption of the PD analysis is that every CH_3CN transitions at the same selected position in the cloud were all considered to share an identical source filling factor. However, as higher excitation is expected to occur in denser and warmer environments, higher-K transitions of higher upper-energy levels may occur readily in more compact regions closer to their corresponding central sources, leading to smaller source filling factors than for the lower-K transitions. Indeed, the evident velocity offsets between the CH_3CN 18_4–17_4 and 18_7–17_7 lines at position B, as shown in Figure 6, may simply reflect the variation of the major emission zone in the cloud as a result of subtle changes in the physical conditions, such as higher gas density and temperature. We note that in fact the derived rotational temperatures and total column densities at positions B, C, and D (Table 4) based on the χ^2 minimization have large uncertainties due to line opacities or the degeneracy of free parameters. Transitions from less populated higher K levels should be optically thin, and if observable, could provide the necessary constraints in the PD analysis.

5.2. Clumpy Nature of Orion KL

It appears that the CH_3CN emission in Orion KL is mostly spatially resolved judging from the spectral images (Figure 1). As discussed in Section 5.1, the best-fit source-filling factors (Table 4) are much smaller than unity, with their maximum value less than one half. One possible explanation for the inferred small filling factors is that the apparently resolved source structures seen in Figure 1 are actually an ensemble of *clean*-beam convolved small clumpy components of size less than our arcsecond beam. Such an argument is supported, for instance, by the early VLA images of NH_3 which did show clumpy features close to IRc2 at $1''$ resolution (Migenes et al. 1989), and by the continuum components seen toward the Orion KL Hot Core when observed with a sub-arcsecond beam (Beuther et al. 2004). When analyzing the observed CH_3OH lines, Beuther et al. (2005a) also suggested source filling factors as small as of 0.14–0.3 within their arcsecond beam for the CH_3OH gas in Orion KL.

Another possible explanation for small source-filling factors in Orion KL could be related to the missing flux in our interferometric observations. As noted previously, ~65%–35% of the spectral flux density was missing for the 18_K–17_K transitions from $K = 0$ to $K = 8$, accordingly. The small source-filling factors inferred thus could be partly due to missing flux problem. Consequently, the beam-averaged upper-state column density, N_u, derived for each transition would be underestimated. Future sub-arcsecond imaging of molecular emission will be necessary to explore the true clumpy nature of the Orion KL gas cloud.

5.3. Kinetic Temperature

The PD analysis assumes LTE which require the gas density be high enough to thermalize the level populations (Goldsmith & Langer 1999). The critical densities, defined as $n_{\rm crit} = A_{\rm ul}/C_{\rm ul}$ where $C_{\rm ul}$ is the collisional coefficient in $\rm s^{-1}$ $\rm cm^3$ and $A_{\rm ul}$ can be obtained from Equation (5), of the CH_3CN $J = 18$–17 transitions were estimated to be around 10^7 $\rm cm^{-3}$ at $T_{\rm kin} =$ 100 K following Green (1986). Thus, a gas density of molecular hydrogen, H_2, higher than 10^7 $\rm cm^{-3}$ is essential to thermalizing the $J = 18_K$–17_K emission. In comparison, the $n_{\rm crit}$ of CH_3CN $J = 5_K$–4_K transitions (Wilner et al. 1994) were found to be about only 10^5 $\rm cm^{-3}$ at 100 K.

Based on the observed 331-GHz continuum of thermal dust emission in Orion KL, we estimated a lower limit (with the consideration of missing flux) of total mass of molecular hydrogen to be about 0.48 $M_\odot$ over a $5'' \times 5''$ region centered at the Orion Hot Core by assuming the continuum emission is optically thin, a grain size of 0.1 μm, a grain mass density of 3 g $\rm cm^{-3}$, a gas-to-dust mass ratio of 100 and a spectral index β of 1.6. Here a dust temperature of 300 K was adopted (Beuther et al. 2005b). This corresponds to an H_2 number density of about 1.4×10^7 $\rm cm^{-3}$ distributed uniformly over a $5''$ diameter sphere. Similarly, an H_2 number density of about 0.7×10^7 $\rm cm^{-3}$ was found distributed uniformly over a region $5''$ in size toward the Compact Ridge. Therefore, the LTE condition assumed for the analysis of the observed CH_3CN emission toward Orion KL appears to be a reasonable approximation, and the derived rotational excitation temperature of CH_3CN transitions can be thus taken as the gas kinetic temperature.

Toward the Orion Hot Core, two locations, positions A and B, were selected for CH_3CN excitation analysis. At position A, the line profile of each K-ladder line is primarily single-peaked, though the line profiles of $K = 7$ and $K = 8$ transitions appear to be skewed toward redshifted side, implying there might exist two slightly different velocity components at higher excitation. However, an apparent double-peaked line profile can be seen at each K transition at position B. From the PD analysis, we found that the redshifted component, at $V_{\rm LSR} = 10.3$ km $\rm s^{-1}$, has an excitation temperature of ~620 K, significantly higher than that of the blueshifted component at ~330 K at $V_{\rm LSR} = 4.3$ km $\rm s^{-1}$. The excitation temperature of ~190 K, obtained at position A at $V_{\rm LSR} = 5.5$ km $\rm s^{-1}$, on the other hand, was found to be close to the temperature at position $B_{\rm blue}$ if the uncertainty is taken into account. Together with the fact that both cloud components at positions A and $B_{\rm blue}$ do exhibit similar LSR velocities, a reasonable assumption thus followed is that these two cloud components may be physically associated with each other in the Hot Core region. The newly detected dust component SMA1 nearby, which was later suggested to be a very young intermediate- to high-mass protostar that powers the wide-angle NW-SE outflow (Beuther et al. 2004, 2008), may be responsible for the CH_3CN excitation at position B.

Compared to early single-dish and interferometric observations of Orion KL (Loren & Mundy 1984; Sutton et al. 1986; Wilner et al. 1994; Wilson et al. 2000; Beuther et al. 2005a), the kinetic temperatures we obtained are generally consistent with those early results. For the Hot Core, they are generally hotter than those found for the lower J CH_3CN lines (~120 K; Andersson et al. 1984) and for ammonia (~115 K; Hermsen et al. 1985). The combination of high-excitation CH_3CN transitions and the arcsecond resolution, however, allows us in principle to sample denser and warmer regions than did the early single-dish observations. Wilner et al. (1994) derived a lower limit of the gas kinetic temperature in the Hot Core to be $\gtrsim 250$ K at $7\farcs3 \times 5\farcs1$ resolution. With arcsecond resolution, we measured a gas kinetic temperature in the range of 190–620 K toward the Orion Hot Core. The seemingly lower kinetic temperature derived by Wilner et al. (1994) could result from averaging over a larger beam area, as it is now apparent (Table 4) that the temperature distribution is not really uniform, even on small angular scales. At ~1″ resolution, Wilson et al. (2000) reported an image of rotation temperature (130–170 K) derived with the ratio over two transitions from the data between 4.4 km $\rm s^{-1}$ to 6.8 km $\rm s^{-1}$. However, with higher spectral resolution, the single Gaussian-like spectra observed in NH_3 can be decomposed into two velocity components as seen in our data. Indeed, the two-zone model over a 43″ beam implied a hotter component at ~400 K. As a result, our multi-line measurement is consistent with the line ratio method by Wilson et al. (2000) if errors are considered. Similar results are reported by Beuther et al. (2005a) from CH_3OH lines at arcsecond resolution, especially the small source filling factors implied from optically thick transitions.

At position C near the infrared source IRc7, the CH_3CN line profile is double-peaked with the blueshifted component at $V_{\rm LSR} = -0.4$ km $\rm s^{-1}$ and the redshifted one at $V_{\rm LSR} =$ 5.6 km $\rm s^{-1}$. This redshifted component, though with an excitation temperature lower than that of the Hot Core, does display an LSR velocity similar to those at positions A and $B_{\rm blue}$ in the Hot Core region. The infrared source IRc7, which was found to be compact and prominent in mid-IR suggesting a relatively early phase of star formation (Gezari et al. 1998; Greenhill et al. 2004), is likely accountable for the excitation of CH_3CN at position C. Using the PD analysis, we found that the CH_3CN column density cannot be reasonably constrained for $C_{\rm red}$ due to large line opacities implied in most of the CH_3CN K-ladder transitions. The derived high source-averaged column density of $\sim 3 \times 10^{17}$ $\rm cm^{-2}$ suggests strongly that the $C_{\rm red}$ cloud component is probably in a region of high gas density where star formation may soon happen.

Toward the northern part of Compact Ridge at positions D and E, kinetic temperatures in the range of 170–280 K were derived, consistent with the temperatures found in early studies (Loren & Mundy 1984; Wilner et al. 1994). The infrared source IRc4 is near position D and IRc5 is near position E; these two IRc sources may have contributed to the excitation of CH_3CN at positions D and E, respectively. Similar LSR velocities between $C_{\rm blue}$ and $D_{\rm blue}$ may imply a common origin of these two spatial components in the gas cloud.

5.4. Kinematics: Semi-open Cavity Structure in Orion KL

As can be readily seen in Figure 1, the CH_3CN emission is distributed in NE-SW direction from the Hot Core toward the Compact Ridge. Such elongated emission structure is in fact an ensemble of complicated velocity components as shown in the channel maps (e.g., Figure 2). The gas motion near the Compact Ridge disclosed by CH_3CN emission, together with the more detailed P–V diagram analysis (Figure 4), suggests the existence of a semi-open cavity structure in the region between the Hot Core and the Compact Ridge (Section 4.3). Here we further propose that this semi-open cavity-like structure is caused by the low-velocity outflow in the SW direction from the Hot Core region.

Methyl cyanide is known to have a large permanent dipole moment which makes it a good high-density tracer, thus it could be helpful for tracing the dense entrained gas swept-up by the outflow (Figure 8). The double-peak line profiles seen at sample

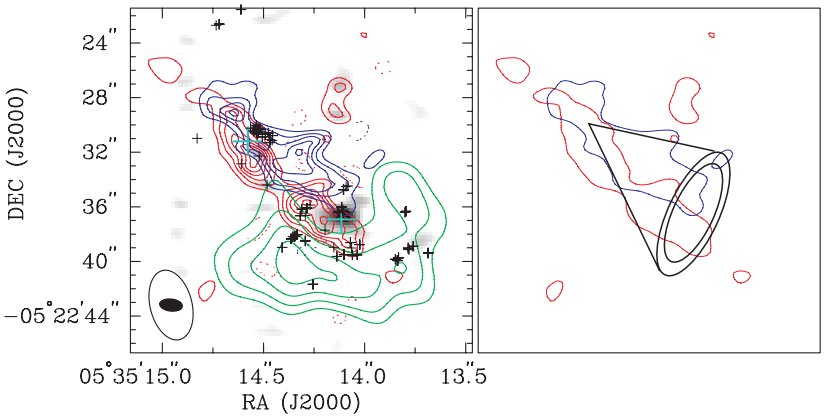

Figure 8. Low-density semi-open gas cavity in the Orion KL cloud core. Left: the spatial distribution of some key molecular emission observed. The blueshifted (V_{LSR} = −5–+5 km s^{-1}) component of CH_3CN 18_3–17_3 emission is shown in blue contours, and in red contours for the redshifted CH_3CN emission (V_{LSR} = +5–+15 km s^{-1}). In addition, also shown is the $HCOOCH_3$ $11_{8,3}$–$10_{7,3}E$ emission (denoted in grey scale) and HCOOH emission taken from Liu et al. (2002; in green contours) superimposed with the CH_3CN spectral image. Blue and red contours start at 3σ with 2σ steps with an rms of 0.8 Jy beam^{-1}. Green contours are plotted at 45%, 60%, 75%, and 90% of the value of HCOOH peak emission. Synthesized beams are of ∼1.″6 × 0.″9 in size for CH_3CN and $HCOOCH_3$ emission (filled ellipse) and of 5″ × 3″) for HCOOH observation (open ellipse). Crosses in indigo color indicate the continuum peak of the Hot Core and the $HCOOCH_3$ emission peak. Crosses in black mark the locations of water masers observed by Gaume et al. (1998). Right: a schematic cartoon of the proposed southwest gas outflow originated from the region near the Hot Core. The cavity structure located between the Hot Core and the Compact Ridge is evident in the SW outflow cone illustrated.

positions B, C, and D may reflect the two velocity components of the southwest wide-angle outflow: one represents the near-side velocity component and the other represents the far-side velocity component. In addition, we could separate the overall CH_3CN emission into two velocity ranges: one is from V_{LSR} = −5 to +5 km s^{-1}, and the other, from +5 to +15 km s^{-1}, as shown in blue and red contours, respectively, in Figure 8 (left). Also plotted in the figure is the integrated intensity map of $HCOOCH_3$ $11_{8,3}$–$10_{7,3}$ E (in gray scale), superimposed with the spectral image of HCOOH taken from Liu et al. (2002; in green contours). Near the Compact Ridge, the spatial distribution of the blueshifted and redshifted CH_3CN emission is obviously different from each other—CH_3CN emission at these two separate velocities appears to encompass the $HCOOCH_3$ emission zone from its north and east. Furthermore, our high-resolution SMA observations demonstrated distinctly that $HCOOCH_3$ emission is located exactly at the spot void of HCOOH emission (Figure 8, left). The large CH_3CN line widths, FWHM ∼4–7 km s^{-1} (see also Figure 4), at the sampled positions denote the CH_3CN gas in the swept-up entrained gas is highly turbulent. Figure 8 (right) shows the schematic picture of the proposed SW cone-like outflow. Gaume et al. (1998) observed many water maser spots around the end opening of the presumed outflow cone. The SW cone appears to point toward us slightly out of the plane of sky with an inclination angle close to zero. The similarity of the position angles between the SiO images (Beuther et al. 2005a) and our CH_3CN images suggests that the driving source of this SW cone-like structure may be from source I. We note the CH_3CN emission near the source I is weak which may imply the destruction of CH_3CN due to energetic process by source I (Wilson et al. 2000). Though it is close to the Hot Core position, the actual driving source of the proposed SW gas outflow cannot be determined unambiguously based on our CH_3CN data alone. Recently, Beuther et al. (2008) proposed that SMA1 may be the driving source of the wide angle outflow in the NW-SE direction. In such a picture, our CH_3CN data may simply trace the entrained gas from the turbulent environment and the apparent semi-open cavity is line-of-sight coincident of gas clumps between the Hot Core and the Compact Ridge.

5.5. Fractional Abundances

Adopting H_2 column densities of 8.8 × 10^{23} cm^{-2} and 1.9 × 10^{23} cm^{-2} for the Hot Core and Compact Ridge, respectively (Wright et al. 1996), we derived CH_3CN fractional abundances of (1–4)×10^{-8} toward the Hot Core and (3×10^{-8})–(1×10^{-7}) at the Compact Ridge.[6] Near IRc7, an assumed H_2 column density of 8.8 × 10^{23} cm^{-2} (Wright et al. 1996) yields a fractional abundance of 8 × 10^{-9} for the blueshifted gas component at position C, C_{blue}, and an abundance of 2×10^{-8} for the redshifted component, C_{red}. Such high CH_3CN fractional abundances of a few ×10^{-8} have also been reported toward Sgr B2(N) (Nummelin et al. 2000).

Chemical models of the Orion KL region usually consider that the evaporation of molecular ice mantles from dust grains plays a dominant role in setting the composition (Blake et al. 1987; Charnley et al. 1992; Caselli et al. 1993; Rodgers & Charnley 2001). The question then is whether CH_3CN is evaporated as a mantle constituent or synthesized in the hot gas, post-evaporation. The detection of CH_3CN in comets (e.g., Biver et al. 2002) is evidence for its presence in astronomical ices, however its origin in these objects is unclear and may be more related to chemistry in nebular gas, or to the possibility that cometary ices underwent a higher degree of processing than interstellar ices (e.g., Charnley & Rodgers 2008).

In cold gas phase interstellar chemistry, CH_3CN can be produced through the radiative association of CH_3^+ and HCN to form CH_3CNH^+, followed by electron dissociative recombination. Observations, however, indicate that methyl cyanide in the cool dense gas which eventually forms protostars has an abundance of ∼10^{-10} (Ohishi & Kaifu 1998), significantly lower than what have been inferred here in Orion KL. Hence, evaporation of CH_3CN frozen out prior to the hot core phase (Brown et al. 1988) cannot be the source of the molecules we observed.

Alternatively, CH_3CN might form in situ on grain surfaces. For this to be the case, methyl and cyanide functional groups are

[6] The beam-averaged column densities were used in deriving fractional abundances in order to preserve the uniformity as much as possible among various sample positions for comparison purpose, as source filling factors varied at different locations. Same H_2 column density was applied to the different velocity components for a given line of sight.

probably required to be associated on the surface (e.g., Hollis & Churchwell 2001). While there certainly appears to be a need for methyl formate ($HCOOCH_3$) to be formed through reactions of HCO and CH_3O surface radicals (e.g., Garrod & Herbst 2006), it is debatable whether or not such an origin could be extended to CH_3CN.

If both $HCOOCH_3$ and CH_3CN form contemporaneously on dust in this manner, as has been proposed recently (Garrod et al. 2008; Belloche et al. 2009), then we might expect that, upon desorption, they should both be present in the same hot gas. Thus, observationally, $HCOOCH_3$ and CH_3CN emission from transitions of similar excitation should exhibit closely matched spatial distributions. This is in contrast to the well-known general anti-correlation between complex O-bearing and N-bearing molecules (e.g., Blake et al. 1987; Liu et al. 2002; Beuther et al. 2005a). Specifically, recent interferometric maps of the Orion KL region with the SMA and CARMA indicate that $HCOOCH_3$ emission is strongest near the Compact Ridge and IRc5. When compared to the CH_3CN $J = 18$–17 $K = 0$ and $K = 1$ maps in Figure 1, which have $E_u = 151, 158$ K, the $HCOOCH_3$ ($20_{1,19}$–$19_{1,18}$ A) emission ($E_u = 120$ K; Friedel & Snyder 2008), $HCOOCH_3$ ($11_{8,3}$–$10_{7,3}$ E) emission ($E_u = 81$ K; Figure 8), and $HCOOCH_3$ ($28_{10,19}$–$27_{10,18}$) emission ($E_u = 307$ K; Beuther et al. 2005a), clearly do not follow that of CH_3CN. Thus, CH_3CN is not formed in grain-surface chemistry.

Evidently, the high abundances of CH_3CN observed must be produced in the hot gas after mantle evaporation has occurred. Rodgers & Charnley (2001) showed that N/O chemical differentiation in hot cores is primarily a temperature effect. Above about 200 K, oxygen atoms and hydroxyl molecules are largely converted to water; this lack of reactive oxygen means that an N-rich chemistry can occur. High abundances of HCN can quickly be formed under these conditions and enhanced CH_3CN abundances of $\sim 2 \times 10^{-7}$ follow from this. These model calculations show that CH_3CN production is optimized at the highest temperatures ($\geqslant$300 K) and when NH_3 is injected from the ice mantles. Observations of Orion KL tend to support this picture. A connection between methyl cyanide emission and dust is supported by our 331 GHz continuum observations (Figure 1(a)). Furthermore, we also found the CH_3CN distribution observed by the SMA is similar to the NH_3 distribution observed by the Very Large Array (Wilson et al. 2000). Together with the high temperatures derived from our CH_3CN observations, these observations support an origin of methyl cyanide by high temperature gas-phase chemistry in dusty environments. In the Compact Ridge, lower temperatures and dust concentrations were observed. In this case, the CH_3CN molecules may have been transported to the Compact Ridge in a low velocity outflow from the Hot Core region—a scenario that has been explored previously in the context of other molecules (Blake et al. 1987; Millar et al. 1991).

6. CONCLUSIONS

We observed CH_3CN $J = 18$–17 transitions in the Orion KL molecular cores with the SMA. At a resolution of $1\farcs6 \times 0\farcs9$, complex gas structure and excitation conditions are revealed. The overall CH_3CN emission is confined within $\sim 15''$ region including the Hot Core, the Compact Ridge, and the Western Clump. Spectra were taken at five representative positions A through E for excitation analysis. Low K lines appear to be optically thick judging from their similar peak intensities. Under LTE conditions, lower limits for the kinetic temperatures in the Orion KL region lie between 45 and 60 K.

As the conventional rotation diagram analysis is inadequate for dealing with large line opacities, we employed the PD analysis and revealed the small-scale inhomogeneous temperature distribution in Orion KL. Toward the Hot Core, the rotational temperatures vary from 190 K to 620 K. The rotational temperatures are 170–280 K near the Compact Ridge. Beam-averaged column densities are $(1$–$4)\times 10^{16}$ cm^{-2} and $(0.5$–$2)\times 10^{16}$ cm^{-2} toward the Hot Core and the Compact Ridge, respectively. Close to IRc7, the rotational temperatures are found to be 100–350 K. The beam-averaged column density is $\sim 0.7 \times 10^{16}$ cm^{-2} for position C_{blue}, and a rough lower limit of column density of $\sim 1.3 \times 10^{16}$ cm^{-2} was derived for position C_{red} due to large line opacities associated with all K-ladder lines. Thus, the average fractional abundance in Orion KL is estimated to be about 10^{-8} to 10^{-7}. Moreover, small source filling factors hence clumpy features in Orion KL are disclosed also with the aid of PD analysis. The apparent resolved source structures are likely an ensemble of smaller clumps with angular size less than $1''$.

A semi-open cavity-like gas structure, which could be likely formed due to the southwest low-velocity outflow originated from the Hot Core region, is inferred to be situated between the Hot Core and the Compact Ridge. The observed CH_3CN gas most likely traces the dense entrained gas swept-up by this low-velocity outflow. Evaporation of grain-mantles followed by chemical reactions in hot gas plays an important role in producing high abundances of CH_3CN. The kinetic temperature structure of Orion KL unveiled by our high-resolution SMA observations will be constructive for future chemical modeling of the Orion cloud core.

The authors thank the anonymous referee for the comments and suggestions to make points more clearly. The authors also appreciate the SMA team for the operation and observations. This work was supported by NSC 96-2112-M-003-012-MY3 grant (Y.-J.K.), by NSC 95-2112-M-001-038-MY2 grant (S.-Y.L.), and by NASA's Exobiology Program and the Goddard Center for Astrobiology (S.B.C.). K.-S.W. thanks ASIAA for the assistantship from 2007 to 2009. The authors are grateful to the JPL Molecular Spectroscopy Web service at http://spec.jpl.nasa.gov for making molecular laboratory data available.

REFERENCES

Andersson, M., Askne, J., & Hjalmarson, A. 1984, A&A, 136, 243
Belloche, et al. 2009, A&A, 499, 215
Beuther, H., Schilke, P., Menten, K. M., Motte, F., Sridharan, T. K., & Wyrowski, F. 2005, ApJ, 633, 535
Beuther, et al. 2004, ApJ, 616, L31
Beuther, et al. 2005, ApJ, 632, 355
Beuther, et al. 2006, ApJ, 636, 323
Beuther, et al. 2008, ApJ, 679L, 121B
Biver, et al. 2002, Earth Moon Planets, 90, 323
Blake, G. A., Masson, C. R., Phillips, T. G., & Sutton, E. C. 1986, ApJS, 60, 357
Blake, G. A., Sutton, E. C., Masson, C. R., & Phillips, T. G. 1987, ApJ, 315, 621
Boucher, D., Burie, J., Bauer, A., Dubrulle, A., & Demaison, J. 1980, J. Phys. Chem. Ref. Data, 9, 659
Brown, P. D., Charnley, S. B., & Millar, T. J. 1988, MNRAS, 231, 409
Caselli, P., Hasegawa, T. I., & Herbst, E. 1993, ApJ, 408, 548
Charnley, S. B., & Rodgers, S. D. 2008, arXiv:0806.3103
Charnley, S. B., Tielens, A. G. G. M., & Millar, T. J. 1992, ApJ, 399, L71
Friedel, D. N., & Snyder, L. E. 2008, ApJ, 672, 962
Garrod, R. T., & Herbst, E. 2006, A&A, 457, 927

Garrod, R. T., Weaver, S. L. W., & Herbst, E. 2008, ApJ, 682, 283
Gaume, R. A., Wilson, T. L., Vrba, F. J., Johnston, K. J., & Schmid-Burgk, J. 1998, ApJ, 493, 940
Genzel, R., & Stutzki, J. 1989, ARA&A, 27, 41
Gezari, D. Y., Backman, D. E, & Werner, M. W. 1989, ApJ, 509, 283
Goldsmith, P. F., & Langer, W. D. 1999, ApJ, 517, 209
Green, S. 1986, ApJ, 309, 331
Greenhill, et al. 2004, ApJ, 605L, 57G
Hasegawa, T. I., Herbst, E., & Leung, C. M. 1992, ApJS, 82, 167
Hermsen, W., Wilson, T. L., Walmsley, C. M., & Batrla, W. 1985, A&A, 146, 134
Hollis, J. M., & Churchwell, E. 2001, ApJ, 551, 803
Liu, S.-Y., Girart, J. M., Remijan, A., & Snyder, L. E. 2002, ApJ, 576, 255
Loren, R. B., & Mundy, L. G. 1984, ApJ, 286, 232
Miao, Y., Mehringer, D. M., Kuan, Y.-J., & Snyder, L. E. 1995, ApJ, 445, L59
Migenes, V., Johnston, K. J., Pauls, T. A., & Wilson, T. L. 1989, ApJ, 347, 294
Millar, T. J., Herbst, E., & Charnley, S. B. 1991, ApJ, 369, 147
Minh, Y. C., Irvine, W. M., Ohishi, M., Ishikawa, S., Saito, S., & Kaifu, N. 1993, A&A, 267, 229
Nummelin, A., Bergman, P., Hjalmarson, Å., Friberg, P., Irvine, W. M., Millar, T. J., Ohishi, M., & Saito, S. 2000, ApJS, 128, 213
O'dell, C. R. 2001, ARA&A, 39, 99
Ohishi, M., & Kaifu, N. 1998, Chemistry and Physics of Molecules and Grains in Space. Faraday Discussions No. 109 (London: The Faraday Division of the Royal Society of Chemistry), 205
Rodgers, S. D., & Charnley, S. B. 2001, ApJ, 546, 324
Sault, R. J., Teuben, P. J., & Wright, M. C. H. 1995, in ASP Conf. Ser. 77, Astronomical Data Analysis Software and Systems IV, ed. R. A. Shaw, H. E. Payne, & J. J. E. Hayes (San Francisco, CA: ASP), 433
Schilke, P., Groesbeck, T. D., Blake, G. A., & Phillips, T. G. 1997, ApJS, 108, 301
Scoville, et al. 1993, PASP, 105, 1482
Shuping, R. Y., Morris, M., & Bally, J. 2004, AJ, 128, 363
Sutton, E. C., Blake, G. A., Genzel, R., Masson, C. R., & Phillips, T. G. 1986, ApJ, 311, 921
Sutton, E. C., Blake, G. A., Masson, C. R., & Phillips, T. G. 1985, ApJS, 58, 341
Turner, B. E. 1991, ApJS, 76, 617
van Dishoeck, E. F., & Blake, G. A. 1998, ARA&A, 36, 317
Willacy, K., Williams, D. A., & Minh, Y. C. 1993, MNRAS, 263, L40
Wilner, D. J., Wright, M. C. H., & Plambeck, R. L. 1994, ApJ, 422, 642
Wilson, T. L., Gaume, R. A., Gensheimer, P., & Johnston, K. J. 2000, ApJ, 538, 665
Wilson, T. L., & Rood, R. 1994, ARA&A, 32, 191
Wright, M. C. H., Plambeck, R. L., & Wilner, D. J. 1996, ApJ, 469, 216